Mechanical fault detection in rotating electrical machines using MCSA-FFT and MCSA-DWT techniques

N. BESSOUS[1]*, S. SBAA[2], and A.C. MEGHERBI[2]

[1]Department of Electrical Engineering, El-Oued University, 39000, El-Oued
[2]Department of Electrical Engineering, Mohamed Khider University, 07000 Biskra

Abstract. This paper presents mechanical fault detection in squirrel cage induction motors (SCIMs) by means of two recent techniques. More precisely, we have analyzed the rolling element bearing (REB) faults in SCIM. Rolling element bearing faults constitute a major problem among different faults which cause catastrophic damage to rotating machinery. Thus early detection of REB faults in SCIMs is of crucial importance. Vibration analysis is among the key concepts for mechanical vibrations of rotating electrical machines. Today, there is massive competition between researchers in the diagnosis field. They all have as their aim to replace the vibration analysis technique. Among them, stator current analysis has become one of the most important subjects in the fault detection field. Motor current signature analysis (MCSA) has become popular for detection and localization of numerous faults. It is generally based on fast Fourier transform (FFT) of the stator current signal. We have detailed the analysis by means of MCSA-FFT, which is based on the stator current spectrum. Another goal in this work is the use of the discrete wavelet transform (DWT) technique in order to detect REB faults. In addition, a new indicator based on the MCSA-DWT technique has been developed in this study. This new indicator has the advantage of expressing itself in the quantity and quality form. The acquisition data are presented and a comparative study is carried out between these recent techniques in order to ensure a final decision. The proposed subject is examined experimentally using a 3 kW squirrel cage induction motor test bed.

Key words: motor current signature analysis (MCSA), discrete wavelet transform (DWT), rolling element bearing faults, rotor eccentricity, stator current spectrum.

1. Introduction

Like most AC motors, induction motors have many advantages of being used in more than 90% when comparing it with other motor types. Their advantage lies in: simple construction, robust and mechanically strong, high starting torque, good speed regulation, operation at high speed without brushes, absence of sparks (useful under hazardous conditions), direct connection to the grid power, squirrel cage rotor of induction motor containing windings which are permanently short circuited, high efficiency with full load, etc. But like any other machine, SCIMs can cause multiple faults under different causes: power imbalance, overvoltage, over-current, overload, construction faults, bad environment, aging of the machine, etc. As per the constituent elements of the SCIM, we quote the percentage defects, as shown in Fig. 1.

This classification depends on the power of the machine to be studied. The distribution of faults on the element bearings, the stator and the rotor show the overall importance of REB faults [24].

We say that monitoring is an essential step to avoid damage, to increase the life of the system, to ensure quality of the product, etc. A rotating machine monitoring is concerned not only with fault detection, but also with how these failures can be detected.
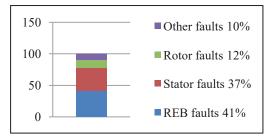

Fig. 1. Percentage distribution of faults in SCIMs

Many techniques are now used in order to detect different faults such as: the eccentricity of the rotor, broken rotor bars, short circuit in the stator and REB faults [5–9].

Massive competition between researchers is accelerating to lead to a simple, efficient and precise technique in the field of diagnosis of rotating machines [10–12]. In addition, several works have focused their efforts on the development of a physically and numerically suitable analytical model [13, 14].

One of the simple techniques that are currently popular in the industry is the vibration analysis, which is based on the vibration image observed in order to analyze its content. This analysis technique is often called motor vibration signature analysis (MVSA) [15, 16]. In fact, the goal of several vibration signal processing methods is to detect faults in rotating machines at the earliest possible stage.

On the other hand, another popular technique is based on the stator coils. They produce a magnetic field that rotates around

the outside of the motor. In addition, the rotor bars produce another magnetic field that influences the stator winding. Air-gap variation leads to a variation in magnetic field distribution (such as e.g. rotor eccentricity).

As a result of the action-reaction phenomenon of the stator and rotor parts, the EMF and current in the stator operate in such a manner that a magnetic field created in the stator will come to act in opposition to the stator magnetic field. Rotor frequency will be linked in the stator with the slip. It can thus be said that the speed of the rotor depends on the difference between rotor and stator frequency, i.e. ($f_s - f_r$). Some harmonics will be induced in both the stator and the rotor as the rotor acts as the frequency converter in the magnitude ($f_s - f_r$ or $f_s + f_r$).

The stator current spectrum is often called motor current signature analysis (MCSA). It is considered one of the many techniques used in diagnosis of rotating machinery. The stator current spectrum by means of the FFT tool is the goal of this study. Our work is based on the REB faults detection by means of the harmonic components verification in the stator current spectrum.

The second technique applied in this sphere is the discrete wavelet transform (DWT). This technique is currently used in many areas: filtering, electrical machine diagnosis, etc. According to the DWT technique, we have defined a new estimator, known as the mean square error (MSE), which checks the existence of REB faults. This indicator has two expressions: a quantitative and qualitative one. In addition, another factor was used in this study which is based on the DWT technique; it is the energy of every detail of this transformation.

The purpose of this paper is the extraction of fault indicators in the stator current signal. First, we did an experimental part which ensures acquisition of the stator current signal. Exploitation by two advanced techniques of signal processing was done by means of analysis of the stator current signal attentively. In addition, a comparative study applied led us to decide on the best choice in an effective manner.

In this regard, the basic principles for REB faults detection using the MCSA and DWT analysis of the stator current signal are explained in the sections below.

2. Motor test bed

The traditional method for measuring different quantities of the electric motor activity is based on an acquisition card and clearly defined measuring devices. But the process of extracting these magnitudes can be difficult to apply in more complicated work positions.

The method of measuring the quantities of electric motor activity requires installation of an adequate test bench. The test bench consists of the motor tested, mounted onto a generator or dynamometer. The motor tested is then connected to the load by a shaft.

This system provides data including current signal, voltage signal and other quantities.
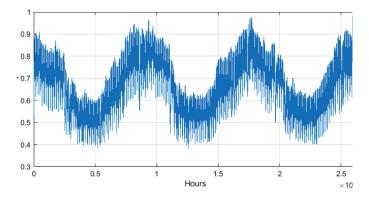

Fig. 2. Experimental setup dedicated to REB faults

In this study, we used SCIM with the following characteristics: 3 kW, p = 2 (number of pole pairs), f_s = 50 Hz and 28 bars. Figure 2 shows the SCIM with some equipment applied in order to take the measurements.

We practically realized two REB fault types. The first is the outer raceway fault (ORF) and the second is the inner raceway fault (IRF). Figure 3 shows photos of healthy and faulty element bearings.

Fig. 3. ORF and IRF

3. MCSA-FFT analysis

3.1. Outer raceway fault detection by MCSA-FFT. Many types of mechanical faults cause oscillations in the load torque applied to the SCIM [17]. We will therefore study the periodic variations effects of the load on the stator current signal under an OR fault. Figure (3) presents a photograph of a bearing defective at the outer raceway. This REB will be installed in the side load of the SCIM. It belongs to the 6206 series.

The stator current spectrum of the SCIM in absence and in the presence of a fault is very rich in harmonics. Indeed, the frequencies presented in this spectrum are mainly the spectral ones related to the characteristic frequencies of REB faults, which are given by [16]:

$$f_{charact-OR, IR, cage, ball}^{\pm} = \left| \nu f_s \pm k f_{OR, IR, cage, ball} \right| \qquad (1)$$

with, $f_{OR, IR, cage, ball}$ being the characteristic frequencies of vibration signal spectrum (MVSA-FFT).

It has been statistically shown in [8] that the characteristic frequencies of the vibration signal can be approximated for most element bearings with ball numbers between 6 and 12 by:

$$f_{OR} = 0.4 N_b \times k \times f_r \tag{2}$$

$$f_{IR} = 0.6 N_b \times k \times f_r \tag{3}$$

where k is any integer, v is the order of the stator time harmonics that are present in the power supply driving the motor ($v = 1, 3, 5$, etc.), f_r is the mechanical rotor frequency and N_b is the number of balls equal to 9.

So, in this case we write:

$$f^{\pm}_{charact-OR-v,k} = \left| v f_s \pm k f_{OR} \right|. \tag{4}$$

We will analyze the stator current spectrum content of the steady-state in both healthy and faulty states when the fault is found in the outer raceway (ORF).

Figures 4 and 5, respectively, represent the spectral content of the stator current for the two operations: at no-load ($s = 0.004 \approx 0$) and at load ($s = 0.04$).

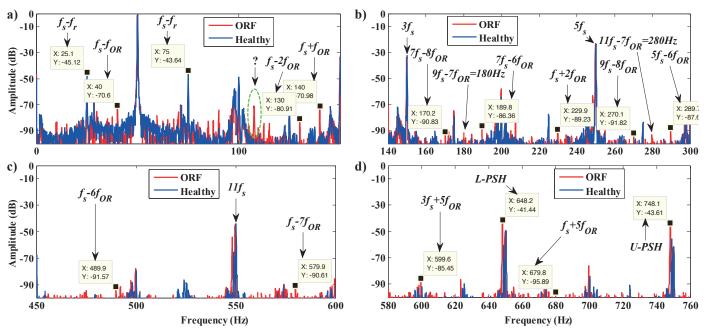We clearly notice the presence of harmonics due to the ORF.

Fig. 4. Stator current spectrum of different frequency bands (ORF, $s \approx 0$): a) 0–150 Hz, b) 140–300 Hz, c) 450–600 Hz, d) Around PSHs
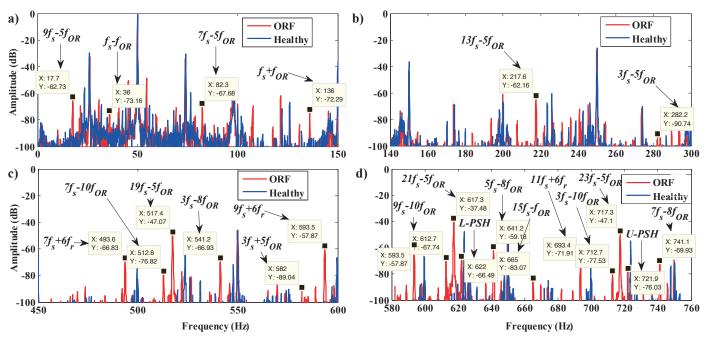

Fig. 5. Stator current spectrum of different frequency bands (ORF, $s = 0.04$): a) 0–150 Hz, (b) 140–300 Hz, (c) 450–600 Hz, (d) Around PSHs

First, and from Fig. 4, we notice the characteristic frequencies of the mixed eccentricity fault around the fundamental frequency: $f_s - f_r = 25.1$ Hz and $f_s + f_r = 75$ Hz. In the [0–150 Hz] band of the figure, we can notice precisely the presence of the peaks around the fundamental frequency, whose frequencies are in agreement with the formula of the characteristic frequencies of equation (5).

$$f_{Mix-ecc} = \left| f_s \pm k f_r \right| \tag{5}$$

The values can be written as follows:

$$f_{charact-OR-1,1}^{-} = f_s - 0.4 N_b \times f_r = 40 \text{ Hz}$$

$$f_{charact-OR-1,1}^{+} = f_s + 0.4 N_b \times f_r = 140 \text{ Hz}$$

$$f_{charact-OR-1,2}^{-} = f_s - 0.4 N_b(2) \times f_r = 130 \text{ Hz}.$$

At the higher orders of the harmonics, we have seen the existence of many series of characteristic frequencies of REB faults along the frequency bands.

This successful comparison of any experimental results with the characteristic frequency formulas of the OR fault allows us to ensure the effectiveness of the diagnostic method for a fault in the element bearings. The Table 1 represents some comparison values between the theory and experimental calculation in no-load operation (s ≈ 0).

Table 1
Theoretical and practical values of harmonics (ORF, $s = 0$)

Formula $f_{charact-OR}^{\pm} = \left\| vf_s \pm k \times f_{OR} \right\|$	Theoretical values [Hz]	Practical values [Hz]	Amplitude [dB]
$\left\| f_s - f_{OR} \right\|$	40	40	−70.6
$\left\| f_s + f_{OR} \right\|$	140	140	−70.98
$\left\| f_s - 2f_{OR} \right\|$	130	130	−80.91
$\left\| f_s + 2f_{OR} \right\|$	230	229.9	−89.23
$\left\| 5f_s - 6f_{OR} \right\|$	290	289.7	−87.7
$\left\| 7f_s - 6f_{OR} \right\|$	190	189.8	−86.36
$\left\| 9f_s - 7f_{OR} \right\|$	180	180	−91.28
$\left\| 9f_s - 8f_{OR} \right\|$	270	270.1	−91.82
$\left\| f_s - 6f_{OR} \right\|$	490	489.9	−91.57
$\left\| f_s - 7f_{OR} \right\|$	580	579.9	−90.61
$\left\| 3f_s + 5f_{OR} \right\|$	600	599.6	−85.45
$\left\| f_s - 7f_{OR} \right\|$	680	679.8	−85.89

Secondly, and in the presence of a slip value (at the load operation), it is clear in Fig. 5 that the ORF has made its mark on the stator current spectrum. Around the fundamental frequency,

we notice the frequencies because of the mixed eccentricity that have the following values: $f_s - f_r = 26$ Hz and $f_s + f_r = 74.1$ Hz.

According to the formula of the characteristic frequencies of ORF $f_{charact-OR-v,k}^{\pm} = \left| vf_s \pm 0.4(k) N_b \times f_r \right|$, we have found what follows:

$$f_{charact-OR-9,5}^{-} = \left| 9f_s - 0.4(5) N_b \times f_r \right| = 18 \text{ Hz}$$

$$f_{charact-OR-7,5}^{-} = \left| 7f_s - 0.4(5) N_b \times f_r \right| = 82 \text{ Hz}$$

$$f_{charact-OR-1,1}^{-} = f_s - 0.4 N_b \times f_r = 36.4 \text{ Hz}$$

$$f_{charact-OR-1,1}^{+} = f_s + 0.4 N_b \times f_r = 136.4 \text{ Hz}.$$

The ORF causes components to appear in the higher frequency of the stator current spectrum. We have shown in figure (5) the spectrum of the stator current in the [580–760 Hz] band. Figutre 6 shows spectral analysis of the current in the [1000–1500 Hz] band; the difference between healthy and faulty state is clearly visible.
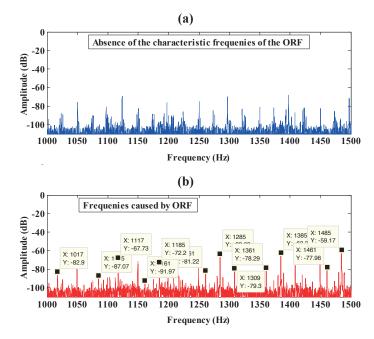

Fig. 6. Stator current spectrum of 1000–1500 Hz frequency bands (s = 0.04): a) Healthy, b) ORF

We notice the appearance of characteristic ORF frequencies, which are located in the frequency range of 1000–1500 Hz and have the following values:

$$f_{charact-OR-11,10}^{-} = \left| 11f_s - 0.4(10) N_b \times f_r \right| = 712.7 \text{ Hz}$$

$$f_{charact-OR-23,5}^{-} = \left| 23f_s - 0.4(5) N_b \times f_r \right| = 717.3 \text{ Hz}$$

$$f_{charact-OR-7,8}^{-} = \left| 7f_s - 0.4(8) N_b \times f_r \right| = 741.1 \text{ Hz}$$

$$f_{charact-OR-21,3}^{+} = \left| 21f_s + 0.4(3) N_b \times f_r \right| = 1309.2 \text{ Hz}$$

$$f_{charact-OR-1,14}^{+} = \left| f_s + 0.4(14) N_b \times f_r \right| = 1159.6 \text{ Hz}.$$

Other sideband frequencies (SBF) caused by this fault are presented in the Table 2:

Table 2
Theoretical and practical values of harmonics (ORF, $s = 0.04$)

Formula $f^{\pm}_{charact-OR} = = \left\| vf_s \pm k \times f_{OR} \right\|$	Theoretical values [Hz]	Practical values [Hz]	Amplitude [dB]
$\left\| 9f_s - 5f_{OR} \right\|$	18	17.7	-62.73
$\left\| 7f_s - 5f_{OR} \right\|$	82	82.3	-82.3
$\left\| f_s - f_{OR} \right\|$	36.4	36	-73.16
$\left\| f_s + f_{OR} \right\|$	136.4	136	-72.29
$\left\| 13f_s - 5f_{OR} \right\|$	218	217.6	-62.16
$\left\| 3f_s - 5f_{OR} \right\|$	282	282.2	-90.74
$\left\| 7f_s - 10f_{OR} \right\|$	514	512.8	$-76.82 \rightarrow 517.8 -2sf_s$
$\left\| 19f_s - 5f_{OR} \right\|$	518	517.4	-47.07 (*SBF*)
$\left\| 3f_s - 8f_{OR} \right\|$	541.2	541.2	-66.93 (*SBF*)
$\left\| 5f_s - 8f_{OR} \right\|$	641.2	641.2	-37.48 (*SBF*)
$\left\| 23f_s - 5f_{OR} \right\|$	718	717.3	-47.1 (*SBF*)
$\left\| 3f_s - 10f_{OR} \right\|$	714	712.7	$-77.53 = 717.3 -2sf_s$
$\left\| f_s + 14f_{OR} \right\|$	1159.6	1161	-91.97
$\left\| 21f_s + 3f_{OR} \right\|$	1309.2	1309	-79.3

Our study has noticed the series of additional frequencies which have severe amplitudes along the harmonic order; these frequencies are due to mixed eccentricity.

In this study, it has been shown that the spectral analysis method of the stator current has given adequate results for ORF. We noticed the efficiency, even around fundamental frequency, whose frequencies are very clear for the induction motor.

Finally, the experimental results obtained confirm compatibility with literature results.

3.2. Inner raceway fault detection by MCSA-DWT. In most cases, the element bearing faults are manifested by: noises, ripples on the contour of the surface of the balls, etc. Meanwhile, the inner raceway fault (IRF) causes many problems in: electromagnetic torque, rotational speed, rotor and stator current, etc. The objective is the detection of IRF by fast Fourier transform (FFT) of the stator current signal.

The different modes of operation used to validate the diagnostic procedure are: no-load operation with a healthy and faulty element bearing and full load operation with a healthy and defective element bearing.

In this first step, we will analyze the stator current in the case when the slip is close to zero (at no-load operation).

Figure 7 shows the presence of harmonics at the frequency of 15.4 Hz, 84.6 Hz, 115.4 Hz, 159.6 Hz and 184.6 Hz around the fundamental value. Moreover, the series of harmonics is verified by the equation below on the illustrated band of [0–1000] Hz.

$$f^{\pm}_{charact-IR-v, k} = \left\| vf_s \pm kf_{IR} \right\|. \tag{6}$$

The frequencies due to the mixed eccentricity are always present in agreement with formula (5), $f_s - f_r = 25.1$ Hz and $f_s + f_r = 75$ Hz among them.
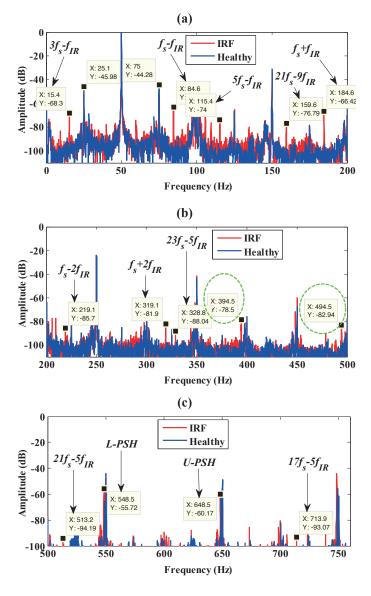

Fig. 7. Stator current spectrum of different frequency bands (IRF, $s = 0.004$): a) 0–200 Hz, b) 200–500 Hz, c) 500–760 Hz

The detection operation by FFT of the stator current made it possible to carry out acceptable monitoring of fault indicators in the IRF.

Moreover, based on the stator current spectrum and according to equation (6), we give some examples of the characteristic frequencies of IRF. Table 3 summarizes and compares theoretical and experimental frequencies in the case of IRF.

Table 3
Theoretical and practical values of harmonics (IRF, $s = 0.004$)

Formula $f_{charact-IR}^{\pm} = \left\| vf_s \pm k \times f_{IR} \right\|$	Theoretical values [Hz]	Practical values [Hz]	Amplitude [dB]
$\left\| 3f_s - f_{IR} \right\|$	15.54	15.4	−68.3
$\left\| 5f_s - f_{IR} \right\|$	115.54	115.4	−74
$\left\| f_s - f_{IR} \right\|$	84.46	84.6	−63.26
$\left\| f_s + f_{IR} \right\|$	184.46	184.6	−66.42
$\left\| 21f_s - 9f_{IR} \right\|$	160.14	159.6	−76.79
$\left\| f_s - 2f_{IR} \right\|$	218.92	219.1	−85.7
$\left\| f_s + 2f_{IR} \right\|$	318.92	319.1	−81.9
$\left\| 13f_s - f_{IR} \right\|$	515.54	513.2	−94.13
$\left\| 17f_s - f_{IR} \right\|$	715.54	713.2	−93.07

According to this table, we can say that the frequency bands that we have analyzed are likely to generate information on the existence of the IR fault.

Slip plays an important role in the calculation of harmonics; it depends, systematically, on the variation of the load. Fig. 8 shows the spectrum of the current under full load operation,

Table 4
Theoretical and practical values of harmonics (IRF, $s = 0.048$)

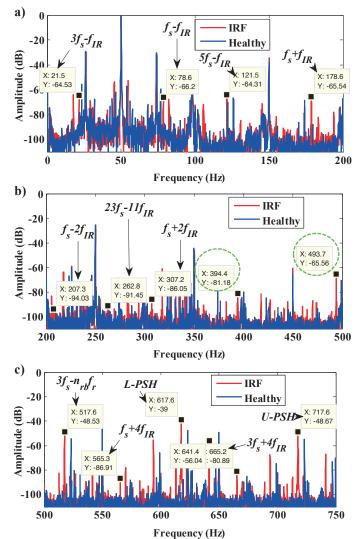| Formula $f_{charact-IR}^{\pm} = \left\| vf_s \pm k \times f_{IR} \right\|$	Theoretical values [Hz]	Practical values [Hz]	Amplitude [dB]
$\left\| 3f_s - f_{IR} \right\|$	21.48	21.5	−64.53
$\left\| 5f_s - f_{IR} \right\|$	121.48	121.5	−64.31 (if not alone, with healthy state = −70.08)
$\left\| f_s - f_{IR} \right\|$	78.52	78.6	−66.2
$\left\| f_s + f_{IR} \right\|$	178.52	178.6	65.54
$\left\| f_s - 2f_{IR} \right\|$	207.04	207.3	−94.03
$\left\| f_s + 2f_{IR} \right\|$	307.04	307.2	−86.05
$\left\| 23f_s - 11f_{IR} \right\|$	263.73	262.8	−91.45
$\left\| f_s + 4f_{IR} \right\|$	564.08	565.3	−86.91
$\left\| 3f_s + 4f_{IR} \right\|$	664.08	665.2	−80.4

Fig. 8. Stator current spectrum of different frequency bands (IRF, s = 0.048): a) 0–200 Hz, b) 200–500 Hz, c) 500–750 Hz

whose slip is equal to 0.048. It shows that around the fundamental frequency, there are other particular harmonics in the spectrum which can confirm the existence of IRF. The calculated values of these harmonics are:

$$f_{charact-IR-3,1}^{-} = \left\| 3f_s - 0.6 \times (1) \times N_b \times f_r \right\| = 21.48 \text{ Hz}$$

$$f_{charact-IR-5,1}^{-} = \left\| 5f_s - 0.6 \times (1) \times N_b \times f_r \right\| = 121.48 \text{ Hz}$$

$$f_{charact-IR-5,1}^{-} = \left\| 7f_s - 0.6 \times (1) \times N_b \times f_r \right\| = 78.52 \text{ Hz}$$

$$f_{charact-IR-1,1}^{+} = \left\| f_s + 0.6 \times (1) \times N_b \times f_r \right\| = 178.52 \text{ Hz}.$$

According to theoretical calculations obtained in the Table 4, we can say that the frequencies obtained experimentally demonstrate the existence of the IRF. These harmonics are more or less readable given the magnitude of realized fault (a small hole).

In this specialized study, we have used the spectral analysis method of the stator current (MCSA-FFT) in order to detect the ORF and IRF in REB of the SCIM. The results that have been obtained are sufficiently acceptable for analysis of the two faults in the REB (ORF and IRF). The signatures are clear along the stator current spectrum, and especially around the fundamental frequency.

4. MCSA-DWT analysis

The signature of a system is the recorded trace as a function of time of these characteristics. This signature must be processed in order to extract the characteristics that make it possible to define the situation of the system at time t.

Various techniques have been exploited, using acoustic analysis, the electromagnetic field, analysis of the motor current, induced voltage, instantaneous power, vibration, etc.

Discrete wavelet transform (DWT) is among the most recent techniques used in fault detection . In addition, this technique is very efficient and greatly enhances the quality of our work because the current sensors are easy to implement and do not require expensive additional transducers.

In this section, we will apply the DWT technique by exploiting the stator current signal. So, the MCSA-DWT technique is used in order to analyze the REB faults. Discrete wavelet transform is considered to be among the best signal processing techniques.

DWT allows us to decompose the signal by means of successive transition from a high-pass filter (HP) and low pass filter (LP). After this operation, we get two coefficients: the approximate a_i and the detail d_i. $a1$ is the approximate shape of the original signal without noise, and $d1$ is the detailed shape of the signal that influences the original signal (noise). Successive operation of this decomposition is represented in the following diagram:
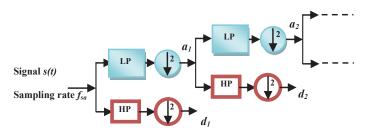

Fig. 9. DWT decomposition process

The Shannon theorem is applied in order to determine the frequency bands of approximations and details. Figure 10 shows the levels of each band.

Higher level decompositions can be obtained based on the Shannon theorem. The frequency band of each level j returns to $\left[0 \rightarrow \frac{f_{sa}}{2^j}\right]$ for approximation bands, and $\left[\frac{f_{sa}}{2^j} \rightarrow \frac{f_{sa}}{2^{j-1}}\right]$ for detail bands. We can stop the process of decomposition by using the following number:
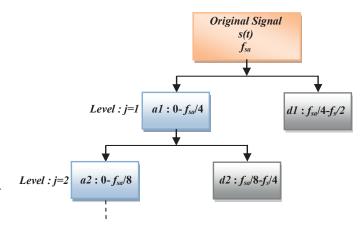

Fig. 10. Decomposition scheme of frequency bands

$$N_{LL} = \text{int}\left[\frac{\log\left(\frac{f_{sa}}{f_s}\right)}{\log(2)}\right] \tag{7}$$

where, f_{sa} is the sampling frequency, and f_s is the fundamental frequency.

[18] proposed a different number of levels for adequate analysis; they used the following formula:

$$N_{LL} = \text{int}\left[\frac{\log\left(\frac{f_{sa}}{f_s}\right)}{\log(2)}\right] + 1 \ or \ 2 \tag{8}$$

[19] has explained the reasons for the choice of this stopping.

For $f_{sa} = 12.8$ k Hz, we find the advisable number of decompositions:

$$N_{Ls} = \text{int}\left[\frac{\log\left(\frac{12.8 \times 10^3}{50}\right)}{\log(2)}\right] + 1 = 9 \ levels.$$

We summarize the frequency bands in the Table 5.

Table 5
Details frequency bands ($f_{sa} = 12.8$ kHz)

Frequency bands of decomposition levels (Hz)	
d_1	3200–6400
d_2	1600–3200
d_3	800–1600
d_4	400–800
d_5	200–400
d_6	100–200
d_7	50–100
d_8	25–50
d_9	12.5–25

The fault indicator can be found at any level. The frequency bands (FB) of each d_i are considered an orientation to the important harmonic values.

In practice, the choice of the wavelet is not crucial. Indeed one seeks a wavelet which offers a good compromise between a temporal and frequency resolution, and such a choice often depends on the objective of the proposed subject. Additional criteria such as regularity, symmetry and rapid decrease at infinity may be necessary.

We have chosen the Daubechies mother wavelet (Db44) for all analyzes concerning this application part [19].

4.1. REB faults detection by Energy-DWT. The energy variation of the details has a very good indicator for SCIM faults. Our study has based on the energy analysis of each detail. We have verified the detail which has a strong influence on the stator current signal.

The energy of detail dj is calculated by:

$$E_j = \sum_{n=1}^{N} \left| d_j(n) \right|^2. \tag{9}$$

N is the total number of samples in the signal and j is the level of detail.

We can calculate the different energies from d1 to d9. We have made a comparison between the two cases: healthy and faulty. Any change indicates the existence of the REB fault. This analysis led us to select the frequency band that is of interest to us.

4.2. REB faults detection by MSE-DWT. Among the methods of distinguishing between signals is the analysis by the mean square error estimator (MSE). This estimator can be used as a quality indicator to give a percentage of resemblance between the X_1 signal and another X_2 signal. Our new approach is based on a study of the correspondence degree between details in order to determine a correct and accurate calculated value (not per vision).

The MSE coefficient of resemblance for two signals X_1 and X_2 (in each position i) which have point numbers n is calculated by the following formula:

$$MSE = \frac{\sum_{i=1}^{n}(X_{1,i} - X_{2,i})^2}{n}. \tag{10}$$

This indicator was used for details di to determine the frequency band on the one hand, and for the determination of the dominant detail in the new signal. Our fault analysis is based on the MSE for detail signals or approximations. The resemblance of the signals is checked for an MSE value that tends towards zero.

4.3. Outer raceway fault detection by DWT. Figures 11–14 represent the detail and approximation signals (d7, d8, d9 and a9) obtained by means of multi-decomposition under ORF for different conditions. The calculation of the relative energy associated with each level of decomposition allows us to differenti-
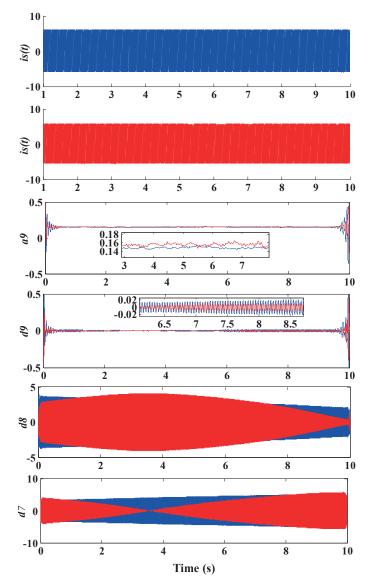

Fig. 11. Multi-level decomposition of stator current at no-load operation: Healthy (in blue), ORF (in red)
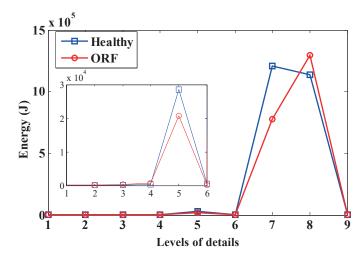

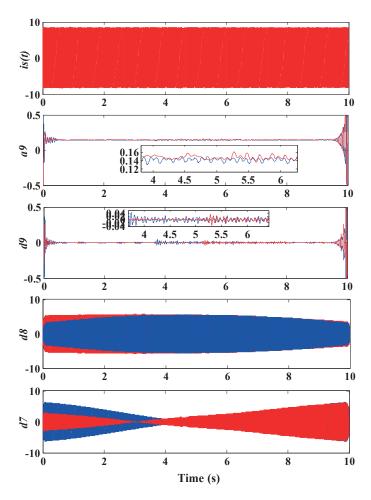Fig. 12. Energy evolution at no-load operation (ORF)

Fig. 13. Multi-level decomposition of stator current at load operation: Healthy (in blue), ORF (in red)
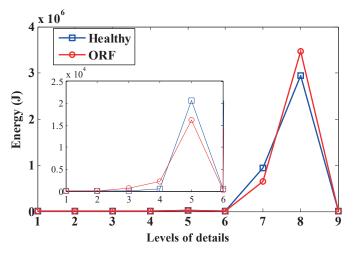

Fig. 14. Energy evolution at load operation (ORF)

of coefficients d7, d8 and d5 is more sensitive as compared to the others. This variation of the amplitude in signals d5, d7 and d8 is due to the fact that the corresponding frequency bands are affected by the defect.

Now, we turn to the fault detection by means of observation and/or comparison between decomposition levels. These details contain a massive amount of information about the state of the machine to be diagnosed. Our proposal focuses on calculation of the MSE value. In addition, it aims to avoid any opposition or overlapping of human opinions on the visual evolution of signals. The tables below show the calculation of MSE values in the presence of ORF.

Table 6
MSE values at different decomposition levels (ORF, $0 \times T_N$)

MSE (di, a9)	MSE value	Resemblance
MSE-d1	3.4938×10^{-05}	Almost present
MSE-d2	5.5600×10^{-05}	Almost present
MSE-d3	0.0028	Less absence
MSE-d4	0.0077	Less absence
MSE-d5	0.2329	Absence
MSE-d6	0.0056	Less absence
MSE-d7	24.9483	Great absence
MSE-d8	19.2467	Great absence
MSE-d9	0.0035	Less absence
MSE-a9	0.0068	Less absence

Table 7
MSE values at different decomposition levels (ORF, $T_N \times 3/4$)

MSE (di, a9)	MSE value	Resemblance
MSE-d1	3.2868×10^{-05}	Almost present
MSE-d2	5.8192×10^{-05}	Almost present
MSE-d3	0.0057	Less absence
MSE-d4	0.0203	Absence
MSE-d5	0.1741	Absence
MSE-d6	0.0066	Less absence
MSE-d7	24.0351	Great absence
MSE-d8	51.1002	Great absence
MSE-d9	0	Present
MSE-a9	0	Present

ate also between the healthy and faulty IM. Figures 11 and 14 show the energy variation of both motors (healthy and faulty state, at no-load and at load operation).

When comparing the detail and approximation signals obtained for machines with defects, we see that the amplitude

The representation of the mean square error evolution for the two types of operations is illustrated in Fig. 15. From Table 7, we see that the detail d9 and the approximation a9 have an excellent similarity (MSE = 0). This value of the MSE = 0

indicates that there will be difficulty in distinguishing between the following two signals:
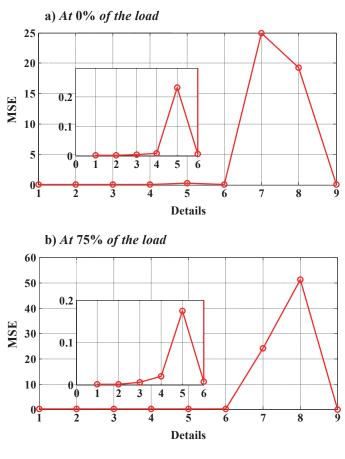- d9-healthy VS d9-with ORF;
- a9-healthy VS a9-with ORF.

a) *At 0% of the load*

b) *At 75% of the load*

Fig. 15. MSE evolution for ORF

4.4. Inner raceway fault detection by DWT. The extraction of information from the stator current in a steady state is generally done during load operation. This choice is necessary because of the difficulty encountered during no-load operation when attempting to extract the information concerning SCIM faults.

The wavelet transform application in the stator current signal is based on the multi-resolution decomposition of the signal.

Figures 16–19 clearly show the evolution of multiple coefficients for different conditions. The effect of the IRF is clear for some coefficient signals and is not clear for others. d7 and d8 are substantially affected by the presence of IR fault.

Calculating the energy stored in each level confirms a decrease observed in detail signals d5 and d8. But we also observe an increase in d7 (17). During load operation, the energy increase was found at detail level d8 only (19). This variation leads us to detect the IR fault and to specify the frequency band. The d7 and d8 bands correspond to the frequencies around 50 Hz.
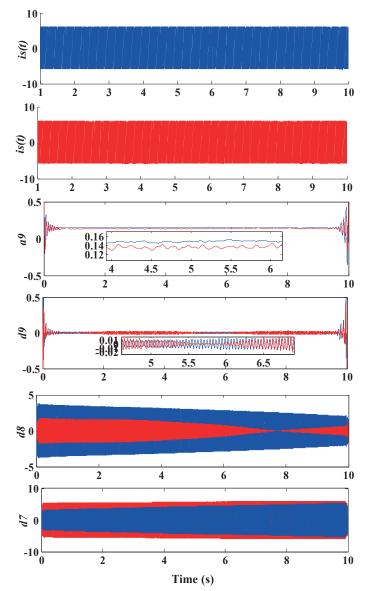

Fig. 16. Multi-level decomposition of the stator current at no-load operation: Healthy (in blue), IRF (in red)
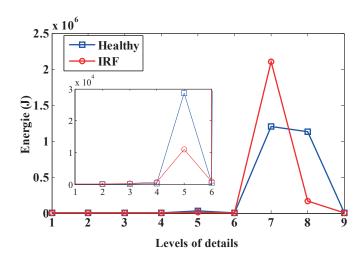

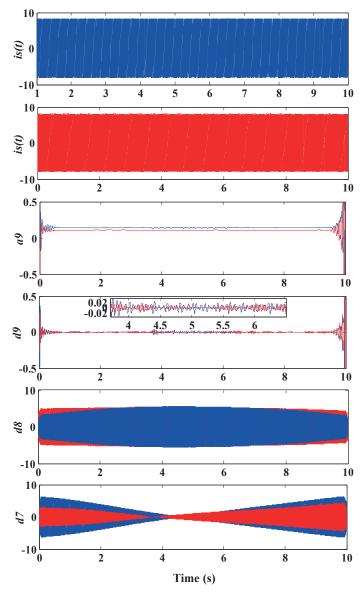Fig. 17. Energy evolution at no-load operation (ORF)

Fig. 18. Multi-level decomposition of the stator current at load operation: Healthy (in blue), IRF (in red)

Fig. 19. Energy evolution at load operation (IRF)
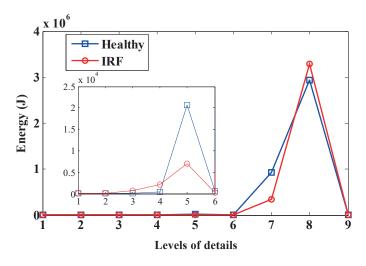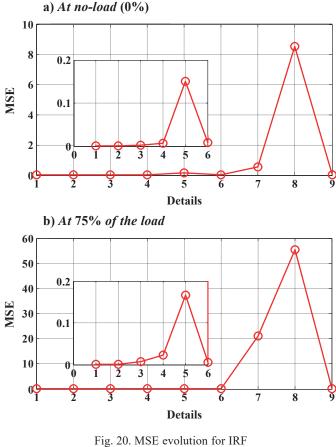
a) *At no-load (0%)*

b) *At 75% of the load*

Fig. 20. MSE evolution for IRF

The analysis by MSE is considered a good indicator which gives a well-defined value for the resemblance or lack thereof between the processed signals. MSE allows us to represent all the information on the resemblance by a single computable and visible value. This aspect of the MSE value is shown in the Table 8 and 9. Figure 20 gives an illustrative summary of the MSE evolution as a function of each detail.

Table 8
MSE values at different decomposition levels (IRF, $0 \times T_N$)

MSE (di, a9)	MSE Value	Resemblance
MSE-d1	2.7053×10^{-05}	Almost present
MSE-d2	6.8581×10^{-05}	Almost present
MSE-d3	0.0029	Less absence
MSE-d4	0.0073	Less absence
MSE-d5	0.1511	Absence
MSE-d6	0.0088	Almost present
MSE-d7	0.5414	Great absence
MSE-d8	8.5167	Great absence
MSE-d9	5.7579×10^{-04}	Almost present
MSE-a9	0.0034	Less absence

Table 9
MSE values at different decomposition levels (IRF, $T_N \times 3/4$)

MSE (di, a9)	MSE Value	Resemblance
MSE-d1	2.9296×10^{-05}	Almost present
MSE-d2	8.3884×10^{-05}	Almost present
MSE-d3	0.0075	Less absence
MSE-d4	0.0229	Absence
MSE-d5	0.1668	Absence
MSE-d6	0.0050	Less absence
MSE-d7	21.1149	Great absence
MSE-d8	55.4360	Great absence
MSE-d9	0.0103	Absence
MSE-a9	0.0511	Absence

5. Conclusion

The observation of stator current signal is a widely used technique. In this study, the motor current signature analysis technique gave good indicators of REB faults. For this reason, MCSA has been preferred until now for fault detection in rotating electrical machines. However, MCSA-FFT does not allow for time-frequency representation as it cannot study the phenomena of the transient regime or the non-stationary signals caused by a variable load.

MCSA-DWT gave precise results on the state of the SCIM. A comparison between the decomposition levels (d_i or a_i) has given us more information about the existence of the fault. A new indicator was introduced in this study; it is the mean square error (MSE) which represents a sound contribution for the final decision in our analysis.

Because of the disadvantages of FFT analysis, many important pieces of information in the non-stationary regime can be exploited more flexibly by means of the wavelet transform (WT) or other techniques.

REFERENCES

[1] W.T. Thomson, "A review of on-line condition monitoring techniques for three-phase squirrel-cage induction motors – past, present and future", in *Proc. IEEE Int. Symp. SDEMPED* 1, 3–18 (1999).

[2] R.K. Patel and V.K. Giri, "Condition monitoring of induction motor bearing based on bearing damage index", *Archives of Electrical Engineering*, 66(1), 105–119 (2017).

[3] L. Saidi, J.B. Ali, E. Bechhoefer, and M. Benbouzid, "Wind turbine high-speed shaft bearings health prognosis through a spectral Kurtosis-derived indices and SVR", *Applied Acoustics* 120, 1–8, (2017).

[4] F.B. Abid, S. Zgarni, and A. Braham, "Distinct Bearing Faults Detection in Induction Motor by a Hybrid Optimized SWPT and aiNet-DAG SVM", *IEEE Trans. En.Conv.* (2018).

[5] A. Głowacz and Z. Głowacz, "Recognition of rotor damages in a DC motor using acoustic signals", *Bull. Pol. Ac.: Tech* 65(2), 187–194 (2017).

[6] B. Rachid, A. Hafaifa, and M. Boumehraz, "Vibrations Detection in Industrial Pumps based on Spectral Analysis to Increase Their Efficiency", *Manag. Syst. .Prod. Eng.* 21(1), 55–61 (2016).

[7] R. Dash and B. Subudhi, "Stator inter-turn fault detection of an induction motor using neuro-fuzzy techniques", *Archives of Control Sciences* 20(3), 363–376 (2010).

[8] C.T. Kowalski, and M. Kaminski, "Rotor fault detector of the converter-fed induction motor based on RBF neural network", *Bull. Pol. Ac.: Tech* 62(1), 69–76 (2014).

[9] R. Valles-Novo, J. de Jesus Rangel-Magdaleno, J.M. Ramirez-Cortes, H. Peregrina-Barreto, and R. Morales-Caporal, "Empirical mode decomposition analysis for broken-bar detection on squirrel cage induction motors", *IEEE Trans. Instr. Meas.* 64(5), 1118–1128 (2015).

[10] A.M. Júnior, V.V. Silva, L.M. Baccarini, and L.F. Mendes, "The design of multiple linear regression models using a genetic algorithm to diagnose initial short-circuit faults in 3-phase induction motors", *Applied Soft Computing*, 63, 50–58 (2018).

[11] G. Singh, and V.N.A. Naikan, "Detection of half broken rotor bar fault in VFD driven induction motor drive using motor square current MUSIC analysis", *Mechanical Systems and Signal Processing* 110, 333–348 (2018).

[12] A. Mejia-Barron, M. Valtierra-Rodriguez, D. Granados-Lieberman, J.C. Olivares-Galvan, and R. Escarela-Perez, "The application of EMD-based methods for diagnosis of winding faults in a transformer using transient and steady state currents", *Measurement* 117, 371–379 (2018).

[13] N. Bessous, S.E. Zouzou, and A. Chemsa, "A new analytical model dedicated to diagnose the rolling bearing damage in induction motors-simulation and experimental investigation," in *Control Engineering and Information Technology (CEIT) IEEE*, 1–9, (2016).

[14] M. Ojaghi and R. Akhondi, "Modeling Induction Motors Under Mixed Radial-Axial Asymmetry of the Air Gap Produced by Oil-Whirl Fault in a Sleeve Bearing", *IEEE Trans. Mag.* (99) (2018).

[15] C. Wang, X. Bao, S. Xu, Y. Zhou, W. Xu, and Y. Chen, "Analysis of Vibration and Noise for Different Skewed Slot-Type Squirrel-Cage Induction Motors", *IEEE Trans. Mag.* 53(11), 1–6 (2017).

[16] C. Kumar, G. Krishnan, and S. Sarangi, "Experimental investigation on misalignment fault detection in induction motors using current and vibration signature analysis", in *Futuristic Trends on Computational Analysis and Knowledge Management IEEE*, 61–66 (2015).

[17] A. Ibrahim, "Contribution au diagnostic de machines électromécaniques: Exploitation des signaux électriques et de la vitesse instantanée", Doctoral dissertation, Université Jean Monnet-Saint-Etienne, (2009).

[18] J.A. Antonino-Daviu, M. Riera-Guasp, J.R. Folch, and M.P.M. Palomares, "Validation of a new method for the diagnosis of rotor bar failures via wavelet transform in industrial induction machines", *IEEE Trans. Ind. App.* 42(4), 990–996 (2006).

[19] N. Bessous, S.E. Zouzou, W. Bentrah, S. Sbaa, and M. Sahraoui, "Diagnosis of bearing defects in induction motors using discrete wavelet transform", *International Journal of System Assurance Engineering and Management* 9(2), 335–343 (2018).